Biosensors and Bioelectronics 132 (2019) 105–114

Contents lists available at ScienceDirect

Biosensors and Bioelectronics

journal homepage: www.elsevier.com/locate/bios

Photo-Sensitive $Pb_5S_2I_6$ crystal incorporated polydopamine biointerface coated on nanoporous TiO_2 as an efficient signal-on photoelectrochemical bioassay for ultrasensitive detection of Cr(VI) ions

Kheibar Dashtian[a], Mehrorang Ghaedi[a,*], Shaaker Hajati[b,*]

[a] Chemistry Department, Yasouj University, Yasouj 75918-74831, Iran
[b] Department of Semiconductors, Materials and Energy Research Center (MERC), P.O. Box 31787-316, Tehran, Iran

ARTICLE INFO

Keywords:
Photoelectrochemical biosensor
$Pb_5S_2I_6$ crystal
Nanoporous TiO_2
Cr(VI) ions
Visible light excitation

ABSTRACT

An ultrasensitive Visible light-triggered photoelectrochemical (PEC) sensor was designed based on ideal photoactive lead sulfoiodide ($Pb_5S_2I_6$) as low band gap crystal, which hydrothermally synthesized rapidly at low temperature (160 °C) in hydrochloride acid media followed by its incorporation into polydopamine as reactive photo-biointerface, through a facile in situ electropolymerization method, coated on nanoporous TiO_2 grown by anodization on Ti foil. The structure of as-prepared samples and their photoelectrochemical properties were fully characterized. This unique photo-sensitive $Pb_5S_2I_6$ catalyst-based PEC bioassay was constructed for the detection of low-abundant Cr(VI) ion in real samples. Applying central composite design, individual and mutual interaction effects were evaluated to obtain optimized solution pH, applied potential and radiant light wavelength as operational factors influencing the PEC efficiency for Cr(VI) detection. At optimal condition, the proposed sensor due to effective suppress in electron–hole recombinations showed a very low detection limit of 3.0 nM, over a broad linear concentration range of 0.01–80 μM in addition to high sensitivity versus 1.9 μA/μM Cr(VI). Proposed PEC sensor displayed high selectivity, reproducibility and stability as well as improved excitation conversion efficiency, which make it highly applicable using solar energy. The potential applicability of the designed sensor was evaluated in water, tomato juice and hair color.

1. Introduction

It has been proven that hexavalent chromium Cr(VI), as an important element for human, is a highly toxic, bioaccumulating, potentially persistent and fiercest environmental nonbiodegradable pollutant because of its increasing utilization in electroplating, the process of cooling towers, burning coal, tanning and sanitary landfills as modern industry and agriculture (Challagulla et al., 2016; Padhi et al., 2017; Khare et al., 2018). Cr(VI) can be combined with DNA, which causes mutations and damages in central nervous system as well as it is very carcinogenic and negatively affects the health even at trace or ultra-trace concentration level (Padhi and Parida, 2014; Jiang et al., 2018). Additionally, consistent with the US Environmental Protection Agency, the threshold limit of Cr(VI) concentration in drinking water is 0.1 mg L^{-1}, which is one of the several reasons on high importance of the accurate detection and determination of Cr(VI) in aquatic organisms or comestible resources, and is meaningful to environmental protection and food security (Fang et al., 2016; Moakhar et al., 2017). Several advanced methods such as atomic absorption spectrometry, electrochemical analysis, inductively coupled plasma mass spectrometry, chromatography and spectrofluorimetry have been developed for detecting and quantifying Cr(VI). However, these methods are time-consuming, unsteady, weakly selective and non-portable in addition to their primarily required separation/pre-concentration procedures and indirect detection systems. Therefore, a fast, facile, sensitive, visual, and pre-screening analytical detection method for the determination of trace Cr(VI) still remains a challenge in the field of environmental monitoring and protection. Recently, photoelectrochemical (PEC) sensing as a new and favorable analytical technique in which the electrons transfer among analytes, photoactive species and electrode after being photoirradiated (Ma et al., 2016; Wang et al., 2016). It possesses several merits such as high integration, low cost and high sensitivity similar to traditional electrochemical sensors, and could effectively be applied for analyte detection (Moakhar et al., 2017). PEC sensing could attain high sensitivity and rapid response via signal amplification by redox-active reporters (Shu et al., 2018, Liu et al., 2016, Shu and Tang, 2017, Yu

* Corresponding authors.
E-mail addresses: m_ghaedi@mail.yu.ac.ir (M. Ghaedi), hajati@mail.yu.ac.ir (S. Hajati).

https://doi.org/10.1016/j.bios.2019.02.042
Received 6 January 2019; Received in revised form 12 February 2019; Accepted 13 February 2019
Available online 22 February 2019
0956-5663/

et al., 2018). In the PEC sensing, photoirradiation excites the active materials on the electrode for enhancing their interaction with analytes (Iyengar, 2017; Li et al., 2017; Ruan et al., 2017; Li et al., 2018; Sui et al., 2019). Despite the advantages mentioned above, surprisingly few studies have been carried out, in this field, for detecting and quantifying Cr(IV). This method, which relies on redox reaction of sensor with electron donor materials presents an indirect PEC Cr(VI) sensor. Generally, in designing a PEC biosensor, it is crucial to select a suitable photoactive and portable material. Titanium dioxide as most common photoactive material has been repeatedly applied as substrate in PEC sensors due to its cost-effectiveness, very good biocompatibility, high surface area, manageable morphology and good stability (Shu et al., 2016; Zhu et al., 2016). Unluckily, TiO_2 is only excitable by UV light, which easily damages any biomolecule (Liu et al., 2018; Shu et al., 2018). Moreover, fast electron-hole recombination in TiO_2 significantly attenuates the TiO_2-based PEC signal and thus limits its applications. The hybrid materials based on the conducting carbon materials, surface loading of noble metals, and multicomponent heterojunctions effectively enhance h^+/e^- charge separation and photoactivity in comparison with TiO_2 (Jang et al., 2017; Xue et al., 2018). Amongst, the use of low band gap semiconductor singly and/or coupled with different morphologies of TiO_2 could effectively result in a tunable absorption band edge, single-photon-generated multiple electrons, long-lasting electron-hole pairs and overall high photoelectrode performances (Shu et al., 2018). Heteroanionic inorganic semiconducting chalco-halides are of considerable attention as ideal optoelectronic functional materials for designing photoelectrodes. Such compounds are of unusual structures because of the distinct bonding favorites of chalcogenide and halide atoms through their competition to occupy a stable site in the structure. Amongst, $Pb_5S_2I_6$ is of mirror-imaged valence and conduction bands, high electron and hole mobility, high dielectric constant, in addition to the fact that its energy band matches that of TiO_2 (Liu et al., 2016; Pathak et al., 2018). Moreover, it is of low rate of recombination of charge carriers (Wang et al., 2015). To the best of our knowledge nowadays, the use of $Pb_5S_2I_6$ based photoelectrochemical sensors has never been reported. Here, a PEC-based sensor was fabricated using binary ideal photoactive thioiodides $Pb_5S_2I_6$ crystal, hydrothermally synthesized rapidly at low temperature (160 °C) in hydrochloride acid media followed by its incorporation into polydopamine (PDA) as reactive biointerface, through a facile in situ electropolymerization method, coated on nanoporous TiO_2 grown on Ti foil (Li et al., 2018). PDA was chosen because of biocompatibility of self-polymerized dopamine, which is easily deposited on different inorganic and organic substrates (Lin et al., 2017; Li et al., 2018; Ren et al., 2018). PDA with conjugated chains results in easy separation of the photo-induced charges and absorbs light over a broad band. Furthermore, it is advantageous that this material is easily prepared and uniformly coated without requiring any high-cost apparatus (Xie et al., 2018). Because of the hydroxyl and amino groups abundantly present in PDA, it directly conjugates with $Pb_5S_2I_6$ as new metal chalco-halide groups via Michael addition reaction without other complicated process, hydrogen bonding and metal complexation. In addition, due to the broadband light absorption of PDA, the proposed PEC sensor exhibited an obvious photocurrent response under visible light and PDA can be played an electron mediator role. The performance of PEC sensor was investigated at different conditions to obtain optimal condition for the detection of Cr (VI). Here, the mechanism of PEC-based Cr(VI) sensing by $Pb_5S_2I_6$, PDA, TiO_2 and Ti foil is demonstrated. The effect of parameters such as solution pH, applied potential and radiant light wavelength on the response was investigated applying small central composite design (SCCD) to evaluate the significance of such parameters and their possible interactions affecting the photocurrent density as response assisted by analysis of variance (ANOVA) (Dashtian et al., 2018a). The optimal parameters, resulting in best response, were found using desirability function (Asfaram et al., 2015; Azad et al., 2016).

2. Experimental

2.1. Materials and apparatus

$K_2Cr_2O_7$, lead chloride ($PbCl_2$), potassium iodide (KI), thioacetamide ($(NH_2)_2CS$), dopamine (DA), HCl, NaOH, polyethylene glycol, ammonium fluoride (NH_4F), Tris buffer, acetone and ethanol were obtained from Merck (Darmstadt, Germany). As received materials were used without any further purification. Phosphate buffered saline (PBS) pellet and 0.3 mm thick Ti foil (99.7%) were acquired from Sigma-Aldrich. Cr(VI) stock solutions (1.0 mmol L^{-1}) were prepared by dissolving $K_2Cr_2O_7$ in DI water followed by its dilution with a nitrogen-assisted deaerated buffer supporting electrolyte (0.1 mol L^{-1} PBS containing 0.01 M TEA (pH 7.0)) to achieve desired concentration of solutions required for running experiments.

Electrochemical impedance spectroscopy, chronopotentiometry, cyclic voltammetry, Mott-schottky, Bode-phase, and chronoamperometry were performed on an AutoLab PGSTAT equipped with a cell including working electrode as well as Ag/AgCl and platinum coil as reference and counter electrodes, respectively. A Metrohm 691 pH meter (Switzerland) was applied to measure the desired pH of working solution, which was set using dilute NaOH or HCl. An electron beam of energy 15.00 keV was applied in field emission scanning electron microscopy (FE-SEM: Sigma, Zeiss, Jena, Germany) to observe the morphology of constituents of the working electrode. The FESEM equipped with energy-dispersive X-ray spectrometry (EDX) detector (Oxford INCA II) of type solid state was applied to acquire the EDX spectrum of $Pb_5S_2I_6$ to obtain its elemental composition. The structure and phase of working electrode constituents were investigated using X-ray diffraction (XRD, PW 1880, Philips, Amsterdam, Netherland) over 2θ range of 10.0–80.0° by CuKα radiation taken at 40 kV and 40 mA. The films were studied by UV–vis diffuse reflectance spectroscopy (UV–vis DRS, Shimadzu UV-2550) to determine their optical characteristics. All photoluminescence (PL) spectra were acquired on a spectrofluorometer (Perkin-Elmer LS 55) exciting at different wavelengths. Other materials, apparatus and software's were applied based on manufacturer instructions as mentioned in our previously published works (Azad et al., 2016; Mosleh et al., 2016a, 2016b, 2016c; Mousavinia et al., 2016).

2.2. Preparation of nanoporous TiO_2 grown on Ti foil

The Ti foil (1.0 × 3.0 cm^2) cleaned by sonicating in ethanol, acetone, 2-propanol and DI water and dried in air was partially anodized to prepare nanoporous TiO_2-coated Ti foil, where a copper foil was used as cathode in a two-electrode electrochemical cell and the anodized sample was horizontally placed on a cooled metallic plate. The anodization was performed in a three-step self-organized way at a potential of 60 V in a polyethylene glycol solution containing NH_4F (0.3 wt%) and H_2O (2.0 wt%) at 20 °C. To protect the oxide layer from the dissolution, the TiO_2 sample was rapidly removed from the cell after the anodization. Afterwards, the sample was rinsed with DI water and dried at 80 °C. Subsequently, to prepare crystalline TiO_2, the obtained amorphous and nanoporous TiO_2 sample was thermally annealed in furnace in air at 525 °C for 2 h. All steps for the preparation of Ti/nanoporous TiO_2 are shown in Scheme S1.

2.3. Preparation of $Pb_5S_2I_6$

Binary ideal photoactive thioiodides $Pb_5S_2I_6$ heterostructure was synthesized as follows: 1.0 mmol of $(NH_2)_2CS$ and $PbCl_2$ together with 2.5 mmol of KI were mixed into 20 mL of 0.8 mol L^{-1} HCl solution. After sonicating the prepared solution for 30 min, it was transferred to a 75 mL Teflon line autoclave and heated at 160 °C in an oven for 10 h. Then, the autoclave was kept at room temperature for being naturally cooled. Finally, a mixture of ethanol and DI water was used to fully wash the samples followed by collecting them.

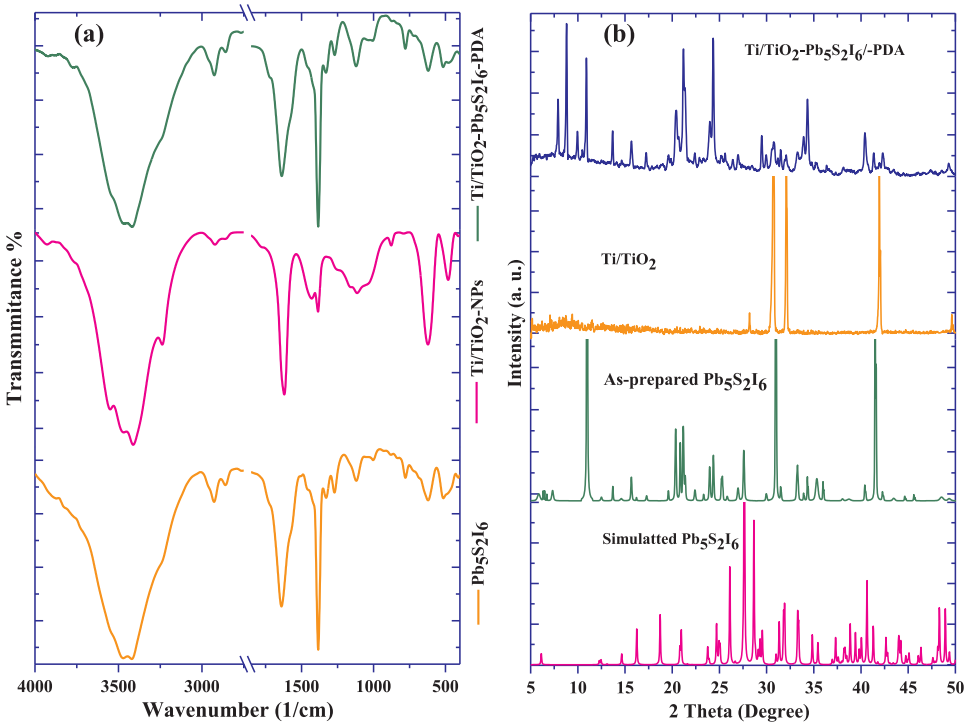

Fig. 1. (a) FTIR spectra of as-prepared $Pb_5S_2I_6$ crystal Ti/TiO_2 and Ti/TiO_2-$Pb_5S_2I_6$-PDA samples and (b) XRD patterns of simulated $Pb_5S_2I_6$ crystal, as-prepared $Pb_5S_2I_6$ crystal Ti/TiO_2 and Ti/TiO_2-$Pb_5S_2I_6$-PDA samples.

2.4. Fabrication of the bio PEC electrode

The PEC electrodes were fabricated by multiple scanning cyclic voltammetry as photoelectrochemical polymerization method for dopamine polymerization in the presence of $Pb_5S_2I_6$ photoactive agent. 20 mg/mL dopamine HCl was prepared in degassed double distillated water, followed by adding and dissolving appropriate amounts of Tris buffer saline solution (TBS, pH 7.4, 3 mg/mL containing 0.01 M TEA), $Pb_5S_2I_6$ (20.0 mg/mL), KCl (0.22 mg/mL) and NaCl (8 mg/mL) by magnetic stirring and nitrogen bubbling for 1.0 h. The solution was then placed in photoelectrochemical cell including Pt counter electrode, Ag/AgCl reference electrode, Ti/TiO_2 working electrode and blue LED as light source. The voltage and scanning rate for the photoelectrochemical reduction of dopamine containing $Pb_5S_2I_6$ onto the Ti/TiO_2 were set to be within the range of 1.5 V to − 1.5 V and at 50 mV/s, respectively. After each cycle, a decrease in the area enclosed with the voltammogram curve was observed due to the deposition of $Pb_5S_2I_6$-containing polydopamine on the Ti/TiO_2 electrode. After 20 cycles, the amount of deposited $Pb_5S_2I_6$-containing polydopamine led to nearly full insulation of the Ti/TiO_2 electrode.

2.5. Samples preparation

Fresh tomato was prepared from local grocery store and its juice was obtained using a household blender. Wastewater samples collected in acid-washed glass bottles were filtered using a 0.45 μm Whatman membrane filter and stored at 4 °C until being analyzed. The solution was adjusted to pH 3.0–4.5 by using a buffer. Hair color was bought from a shop in Yasouj, Iran. Wet digestion of brown color in a 4:1 mixture of per-chloric acid (70–72%) and nitric acid (65%) was performed on a hot plate in fuming hood to get it nearly dried through slow increase in the temperature for 2–3 h. The solution was allowed to be cooled followed by filtering into a calibrated flask (100 mL) using Whatman filter paper no. 45 and storing at 4 °C until being analyzed. The solution was adjusted to pH 3.0–4.5 with an adjustment buffer.

2.6. Design of experiments for electrode composition

Applying CCD, individual and mutual interaction effects of parameters on photocurrent density were evaluated to determine Cr(VI) using the designed sensor (Mosleh et al., 2016a, 2016b). The process of Cr(VI) determination versus independent factors including solution pH (X_1), applied potential (X_2), and radiant light wavelength (X_3) was statistically modeled by SCCD with 15 experimental runs (Table S1). The response (photocurrent density) of the sensor is modeled using the following second-order polynomial versus the above-mentioned parameters:

$$y = \beta_0 + \sum_{i=1}^{4} \beta_i X_i + \sum_{i=1}^{4} \sum_{j=1}^{4} \beta_{ij} X_i X_j + \sum_{i=1}^{4} \beta_{ii} X_i^2 + \varepsilon \quad (1)$$

where y is the predicted response; X_i and X_j are the parameters that independently affect y. The residual of the model is shown by ε and the coefficients of the model are indicated by β_0 (constant), β_i (linear), β_{ii} (quadratic) and β_{ij} (cross-product). The p-values obtained by ANOVA for independent factors and model lack of fit were analyzed to estimate their significance (Mosleh et al., 2016a, 2016b). Moreover, the simplified model after ANOVA was validated by considering difference in fits (DFFITS), cooks distance, contour, 3D surface, leverage, normal plot and residual. The desirability of the model was approved by analyzing the obtained values of R^2, adjusted R^2, predicated R^2, standard deviation (Std. Dev.), adequate precision, coefficient of variation (CV%), mean and predicted residual error sum of squares (PRESS) (Kheirandish et al., 2017a, 2017b, 2017c). Using the desirability function, the optimal condition for determining Cr(VI) ions by the designed PEC sensor was obtained (Kheirandish et al., 2017a, 2017b).

2.7. Photocurrent measurement

The photocurrent was measured using the chronoamperometry under the irradiation of blue light, where the working electrode was set to be the Ti/TiO_2-$Pb_5S_2I_6$-PDA configured in the above-mentioned cell after applying a potential of −0.45 V in an aqueous solution, which

contains a supporting electrolyte, with various concentrations of Cr(VI). The photocurrent was measured in 0.1 M deoxygenated Tris-HCl (pH = 5) buffer containing 0.01 M TEA using an AutoLab electrochemical workstation (302-N, Netherlands).

3. Results and discussion

3.1. Physicochemical characterization

FT-IR was performed to investigate the surface chemical structure of $Pb_5S_2I_6$, Ti/TiO_2 and Ti/TiO_2-$Pb_5S_2I_6$-PDA as well as the binding interactions between the Ti/TiO_2 and $Pb_5S_2I_6$-PDA (See Fig. 1a). In $Pb_5S_2I_6$ spectra, the bands observed over 1400–1650 cm^{-1} are attributed to vibrating O-H group of water molecules absorbed in the material. The 3412 and 3383 cm^{-1} bands indicate the stretching modes of inorganic Pb-I clusters vibrating asymmetrically and symmetrically, respectively. In Ti/TiO_2 spectra peaks at 570 cm^{-1} and 1400 cm^{-1}, could be assigned to the vibrations of Ti–O bonds of TiO_2 nanoporous. Moreover, the asymmetric stretching vibrations of S-O in sulfate species result in 1130 cm^{-1} and 1070 cm^{-1} bands. The disulfides (S-S) stretching causes the bands at 480 cm^{-1} and 600 cm^{-1}. In the Ti/TiO_2-$Pb_5S_2I_6$-PDA spectrum, the band at 3380 cm^{-1} is attributed to the stretching vibrational modes of –OH group of PDA and TiO_2 surface as well as N–H group of PDA. These characteristic bands correspond to the hydrogen bonding between PDA and $Pb_5S_2I_6$. In addition, the narrow bands at 1627 cm^{-1} and 1292 cm^{-1} correspond to C–O and C=O bonds of PDA. Therefore, an electrostatic repulsion originated from the remaining positively charged PDA inhibits the aggregation of $Pb_5S_2I_6$.

All the reflections in XRD pattern of $Pb_5S_2I_6$ (See Fig. 1b) show its monoclinic phase in agreement with JCPDS Card File 23–329, where the observed peaks correspond to the planes of 002, 004, 005, 006, 007, 008, 009, and 0010 (See Fig. 1b). XRD pattern of the as-prepared Ti/TiO_2 (Fig. 1b) corresponds to a pure anatase TiO_2 (JCPDS 21-1272). After the incorporation of $Pb_5S_2I_6$ into electropolymerized PDA followed by its electrodeposition onto Ti/TiO_2 support, all of the peaks mentioned above were observed from Ti/TiO_2-$Pb_5S_2I_6$-PDA XRD pattern (See Fig. 1b). The broad peak observed at 23.0° is assigned to the amorphous PDA (See Fig. 1b). In addition, inductively coupled plasma optical emission spectrometry (ICP-OES) was applied to support the successful preparation of $Pb_5S_2I_6$ after its dissolution in HNO_3/HCl mixture and fully degassing. Quantification by the ICP-OES resulted in the stoichiometry of $Pb_5S_{1.85}I_{6.20}$.

The FE-SEM image of the prepared $Pb_5S_2I_6$ sample (Fig. 2a) showed smooth octahedral crystals in the range 0.2–1.0 μm with hexagonal structure. A porous surface morphology for TiO_2 film on Ti substrate was observed, where the average diameter of connected pores and their neighboring distance were found to be 20 nm and 40 nm, respectively (Fig. 2b). After the incorporation of $Pb_5S_2I_6$ into electropolymerized PDA followed by its electrodeposition onto Ti/TiO_2 support, the morphology of $Pb_5S_2I_6$ was changed to nanorod and was homogeneously dispersed into PDA, confirming the photoelectrode preparation (Fig. 2c).

Furthermore, the elemental analysis was performed by EDX (See Fig. 2), to investigate the contribution of Pb, S and I (Fig. 2d) in $Pb_5S_2I_6$ sample; Ti and O in Ti/TiO_2 sample (Fig. 2e); as well as Pb, S, C, N, I, Ti and O in the photoelectrode (Fig. 2f), confirming its successful preparation. In addition, homogeneous distribution of the mentioned elements within the corresponding samples is shown in Fig. 2.

3.2. Photoelectrochemical characterization

Cyclic voltammograms of bare Ti foil, Ti/TiO_2, and Ti/TiO_2-$Pb_5S_2I_6$-PDA were obtained in presence of 1.0 mM $[Fe(CN)_6]^{3/4}$ containing 0.1 M Tris-HCl (see Fig. 3a). Due to fact that the bare Ti foil is electrochemically inactive, it showed a quasi-reversible and poor characteristic redox peaks, while after its surface oxidation its redox peak current was significantly improved because of enhancement in the process of electron transfer in Ti/TiO_2. Even further enhancement in such parameter was achieved for the Ti/TiO_2-$Pb_5S_2I_6$-PDA suggesting that the Ti/TiO_2-$Pb_5S_2I_6$-PDA nanostructure with highly $Pb_5S_2I_6$ and PDA coverage results in higher electrical conductivity and charge separation at the interface of electrode and electrolyte.

Fig. S1a shows the cycle voltammograms of Ti/TiO_2-$Pb_5S_2I_6$-PDA photoelectrode in 1.0 mM $[Fe(CN)_6]^{3/4}$ containing 0.1 M Tris-HCl at different potential scan rates. The results show that I_p for the oxidation peak is linearly enhanced via increasing υ between 20 and 300 mV/s, which represents a limited surface for this oxidation process (See Fig. S1b). In addition, two linear range relationships between the square root of the scan rate $\upsilon^{1/2}$ and peak current Ip, depicted in Fig. S1c, illustrate that the process for the proposed photoelectrochemical reaction is controlled by diffusion. In other words, it can be said that at low scan rates, the photocurrent is non-propagating, while at high scan rates, the photocurrent is propagating. (i.e. at high scan rates, the mass transfer rate is lower than the charge transfer rate.) Therefore, the reaction is controlled by the mass transfer.

The surface area of the Ti/TiO_2-$Pb_5S_2I_6$-PDA photoelectrode was determined by CV using 1.0 mM $[Fe(CN)_6]^{3/4}$ containing 0.1 M Tris-HCl. Randles–Sevcik equation describes a reversible process as (Rezaei et al., 2015; Biyareh et al., 2018):

$$I_p = 2.69 \times 10^5 n^{2/3} A D^{1/2} C \upsilon^{1/2} \quad (2)$$

where n, I, A, ν, D and C correspond to number of electrons transferred, anodic peak current, surface area of Ti/TiO_2-$Pb_5S_2I_6$-PDA photoelectrode, scan rate, diffusion coefficient and the concentration of $[Fe(CN)_6]^{3/4}$, respectively. For 1.0 mM $[Fe(CN)_6]^{3/4}$ in 0.1 M Tris-HCl electrolyte, $n = 1$, $D = 7.6 \times 10^{-6}$ cm^{-2} s^{-1} (Arvand et al., 2016). The effective surface area of Ti/TiO_2-$Pb_5S_2I_6$-PDA photoelectrode was calculated from the slope of plot of the Ip against $\nu^{1/2}$ and found to be

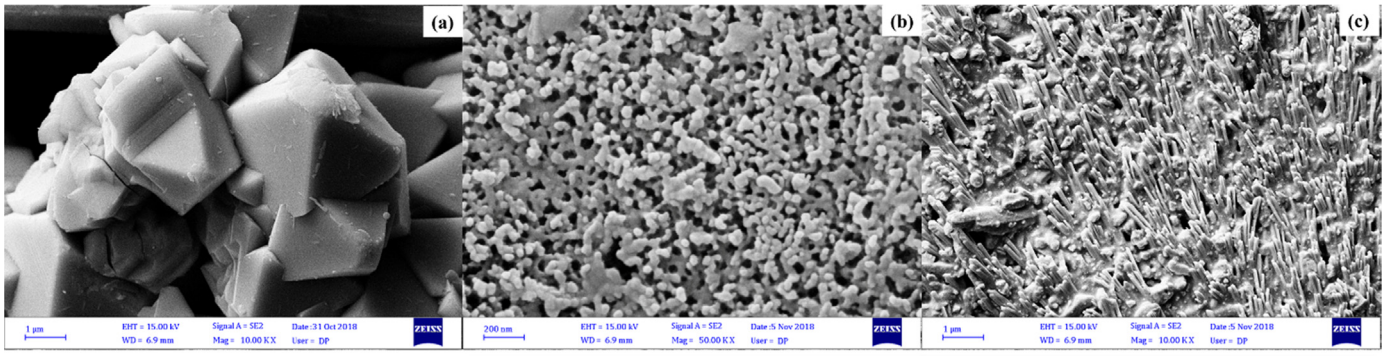

Fig. 2. FE-SEM images of $Pb_5S_2I_6$ crystal (a), Ti/TiO_2 (b) and Ti/TiO_2-$Pb_5S_2I_6$-PDA (c) and EDS spectra of $Pb_5S_2I_6$ crystal (d), Ti/TiO_2 (e) and Ti/TiO_2-$Pb_5S_2I_6$-PDA (f), (homogeneous distribution of constituent elements within each sample is shown below its corresponding spectrum).

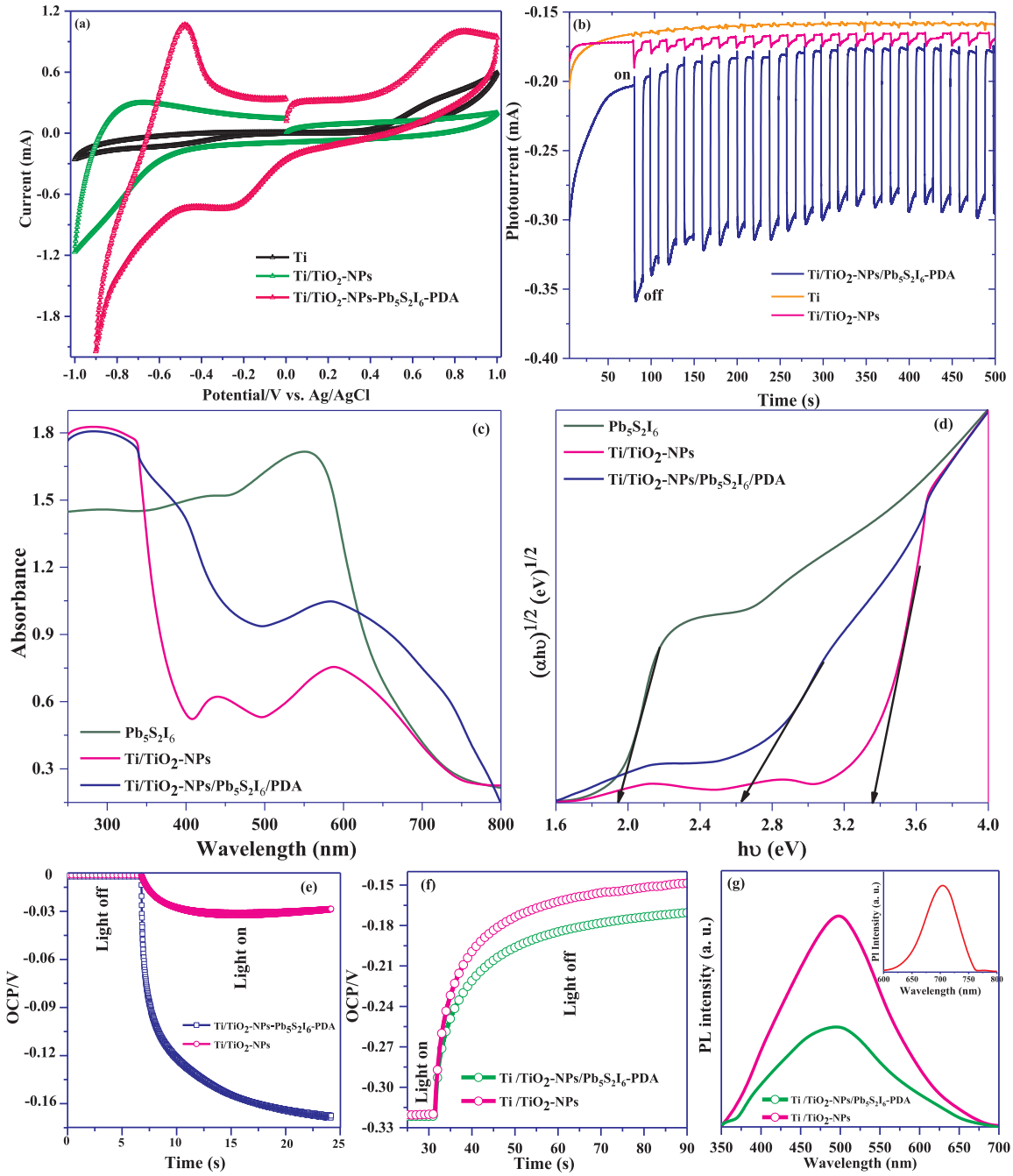

Fig. 3. (a) CVs of as-prepared $Pb_5S_2I_6$ crystal, Ti/TiO_2 and Ti/TiO_2-$Pb_5S_2I_6$-PDA, (b) photocurrent responses of $Pb_5S_2I_6$ crystal, Ti/TiO_2 and Ti/TiO_2-$Pb_5S_2I_6$-PDA in buffer solution, for an applied potential of −0.45 V, (c) UV–Vis DRS spectra, (d) Tauc plots of $Pb_5S_2I_6$ crystal, Ti/TiO_2 and Ti/TiO_2-$Pb_5S_2I_6$-PDA, (d and e) characterizations for charge separation and transfer efficiency: open-circuit potential decay curves (normalized after turning the visible light off) for Ti/TiO_2 and Ti/TiO_2-$Pb_5S_2I_6$-PDA and (f) photoluminescence spectra of Ti/TiO_2 and Ti/TiO_2-$Pb_5S_2I_6$-PDA (b) (see inset for photoluminescence spectrum of $Pb_5S_2I_6$ crystal).

0.356 cm^2 (See Fig. S1a, c). This efficient performance corresponds to good electrical conductivity of $Pb_5S_2I_6$-PDA.

A plot of the peak potential (E_p) vs. the log of the scan rate (logν) (see Fig. S1d) showed a linear relationship represented by the equation $Ep(V) = 0.320\log\nu - 0.156$ with $R^2 = 0.9886$. The peak potential (Ep) varies linearly as a function of the log ν, in agreement with Laviron's theory for an irreversible electrode process:

$$\Delta Ep = -\left(\frac{RT}{anF}\right)\ln\left(\frac{RTk_s}{anF}\right) + \left(\frac{RT}{anF}\right)ln\nu \qquad (4')$$

where E^0 is the formal redox potential, n is the number of transferred electrons, a is the coefficient of charge-transfer, k_s is the heterogeneous electron transfer rate constant, and ν is the scan rate. Thus, the value of "an" was easily calculated to be 0.08 using the slope of Ep vs. log ν (See Fig. S1d). Thus, "a" and the number of electrons transferred in this process were obtained to be 1.0 and 0.079, respectively. In addition, k_s was found to be 1.92 M^{-1} s^{-1} at scan rate of 160 mV/s.

Fig. 3b illustrates the current–time variations corresponding to Ti foil, Ti/TiO_2 and Ti/TiO_2-$Pb_5S_2I_6$-PDA at potential of 0.45 V. On/off switching of blue LED was carried out for 500 s. The steep variation in the photocurrent (acquired from samples) against light on/off switching shown in Fig. 3b (solid line), which is due to the blue light absorption and thus the electron–hole generation shows that the Ti/TiO_2-$Pb_5S_2I_6$-PDA is highly photoelectrochemical active as compared to other

materials. This is because of the effect of high photoactivity of $Pb_5S_2I_6$ and PDA. Since the photoelectrochemical measurements are performed in Tris buffer solution containing 0.01 M TEA, the photocurrent causes from PEC Cr(VI) sensing.

3.3. Optical properties

The DRS spectra of the as-prepared Ti/TiO_2, $Pb_5S_2I_6$, and Ti/TiO_2-$Pb_5S_2I_6$-PDA (Fig. 3c) show high visible light absorbance of $Pb_5S_2I_6$ and Ti/TiO_2-$Pb_5S_2I_6$-PDA. Amongst, the Ti/TiO_2-$Pb_5S_2I_6$-PDA heterostructure showed much better photocatalysis activity because of the presence of PDA and $Pb_5S_2I_6$ as visible-light active species. The energy band gaps of as-prepared Ti/TiO_2, $Pb_5S_2I_6$, and Ti/TiO_2-$Pb_5S_2I_6$-PDA were obtained by the following equation (Dashtian et al., 2018b; Tabatabaei et al., 2018):

$$\alpha h\nu = B(h\nu - E_g)^{n/2} \tag{3}$$

where α, h *and* ν are absorption coefficient, Planck constant and light frequency, respectively; *Eg* and *B* are band gap energy and constant, respectively. Depending on being a direct or indirect bad gap semiconductor, the *n* value is 1 or 4, respectively (Zhang et al., 2018). From the extrapolation of the linear part of the plot of $(\alpha h\nu)^2$ versus ($h\nu$) (Fig. 3d) corresponding to each of the Ti/TiO_2, $Pb_5S_2I_6$, and Ti/TiO_2-$Pb_5S_2I_6$-PDA, their corresponding band gaps were determined to be 3.36, 1.92 and 2.62 eV, respectively. The positions of the conduction band (CB) and valence band (VB) edges of the constituents of the Ti/TiO_2, $Pb_5S_2I_6$, and Ti/TiO_2-$Pb_5S_2I_6$-PDA were estimated by the following equations (Habibi-Yangjeh and Shekofteh-Gohari, 2017):

$$E_{CB} = X - E_c - \frac{1}{2}E_g \tag{4}$$

$$E_{VB} = E_{CB} + E_g \tag{5}$$

where E_{CB} and E_{VB} are the VB and CB edges, respectively. E_c (= 4.5 eV) is free electrons energy vs. NHE. X is the electronegativity of semiconductor, which is determined using Eq. (6).

$$X = [X_{(A)}{}^a X_{(B)}{}^b X_{(C)}{}^c]^{\frac{1}{a+b+c}} \tag{6}$$

where a, b and c are the population of constituent elements in the samples (Pirhashemi and Habibi-Yangjeh, 2015; Habibi-Yangjeh and Shekofteh-Gohari, 2017).

3.4. Charge separation and transfer performances

The separation–recombination behavior of photo-generated charge carries as one of key parameters affects the PEC sensor responses. First, the separation and excitation of electron-holes on the Ti/TiO_2 and Ti/TiO_2-$Pb_5S_2I_6$-PDA surface were investigated (See Fig. 3e). Second, the decay profile of the potential of open circuit was used to study the rate of surface recombination (See Fig. 3f), where its average was determined by the following equation (Thulasi-Varma et al., 2015; Jiang et al., 2018):

$$\tau_n = \frac{-k_B T}{e} dV \left[\frac{dV_{oc}}{dt}\right]^{-1} \tag{7}$$

where k_{BT}, e and dV_{oc}/dt are thermal energy, positive elementary charge and time-derivative of V_{oc}, respectively. It was observed that the Ti/TiO_2-$Pb_5S_2I_6$-PDA has the slowest decay rate of V_{oc} compared to the Ti/TiO_2, suggesting a slower kinetics of recombination and longer lifetime of electron in the Ti/TiO_2-$Pb_5S_2I_6$-PDA. The further study on the rate of separation–recombination of generated charges is carried out by using photoluminescence (PL) spectra (Fig. 3g). As seen, a robust emission at 500 nm in the PL spectrum of Ti/TiO_2 is produced, which can be due to the high recombination rate of the photoinduced electron–hole pairs, while the PL intensity of Ti/TiO_2-$Pb_5S_2I_6$-PDA at 500 nm has been nearly disappeared suggesting an efficient charge separation in the Ti/TiO_2-$Pb_5S_2I_6$-PDA PEC sensor. In addition, the PL spectrum of $Pb_5S_2I_6$ (inset in Fig. 3g) clearly showed an emission at about 710 nm when excited at wavelength of 525 nm, which confirms that the $Pb_5S_2I_6$ strongly absorbs visible light.

3.5. Band Positions of prepared samples

The flat band potential (V_{fb}) as well as the VB and CB measurements for Ti/TiO_2, $Pb_5S_2I_6$, and Ti/TiO_2-$Pb_5S_2I_6$-PDA were carried out by Mott–Schottky experiments. Mott–Schottky is also applied to obtain the donor density and V_{fb} at the interface of semiconductor/liquid. The inverse capacitance-squared and flat band potential correlation for semiconductors of n-type is described using Eq. (8) (Feng et al., 2016):

$$\frac{1}{C^2} = \left(\frac{2}{\varepsilon_r \varepsilon_o e N_D A^2}\right)\left(V_0 - V_{fb} - \frac{KT}{e}\right) \tag{8}$$

where C (F), e (C), ε_r (dimensionless), ε_o (F/m), N_D (m^{-3}) and A (m^2) are capacitance, elementary charge, dielectric constant, free-space permittivity, donor density and electrode geometrical area, respectively. V_0 (V), k (eV/K) and T (K) are extrapolated applied voltage, Boltzmann's constant and temperature, respectively (Zhang et al., 2014). The positive slopes corresponding to Ti, Ti/TiO_2, and Ti/TiO_2-$Pb_5S_2I_6$-PDA clearly indicate that they are n-type semiconductor (Fig. 4a), while the negative slopes corresponding to pure $Pb_5S_2I_6$ show their p-type semiconducting entity (Fig. 4b). V_{fb} of n-type and p-type semiconductors is known to be close to their CB and VB, respectively. V_{fb} values for Ti/TiO_2 and Ti/TiO_2-$Pb_5S_2I_6$-PDA were respectively found to be −0.75 and −0.1 V (vs. SCE), where obtained from the x intercepts of linear region (Fig. 4a). In addition, V_{fb} of pure $Pb_5S_2I_6$ was found to be 1.65 V.

To do more investigation on the internal resistance, recombination behaviors, and kinetics of charge-transfer at interfaces of the prepared samples, electrochemical impedance spectroscopy (EIS) analysis was used at 0.256 V AC signal. The corresponding Nyquist plots (in Fig. 4c) were taken at frequency of 50 kHz. As seen, for bare Ti foil electrode, the impedance spectrum presents a small R_{ct}. When the TiO_2 were grown on the electrode by the anodization, the R_{ct} increased gradually due to weak conductivity of TiO_2. However, the resistance-circle obtained for Ti/TiO_2-$Pb_5S_2I_6$-PDA photoelectrode was found to be lower than that for pristine Ti/TiO_2, which was largely because of the higher electronic conductivity of $Pb_5S_2I_6$-PDA compared to TiO_2. Moreover, the EIS analysis indicates the successful fabrication of the proposed biosensor. Upon photo-irradiation, the valence band electrons of $Pb_5S_2I_6$ get sufficient energy to be injected into the Ti/TiO_2 substrate. Moreover, PDA plays as an electron carrier medium between the above-mentioned materials, and thus the photoelectrode is charged after the transport of the electrons injected in the conduction band, some of which can be simultaneously recombined with the electrolyte followed by reacting with Cr(VI). Therefore, after light illumination on Ti/TiO_2-$Pb_5S_2I_6$-PDA, the R_{ct} decreases gradually due to low electron-hole recombination.

In addition, the lifetime of electron in prepared electrodes was investigated using Bode-phase analysis by Eq. (9) (Wang et al., 2018):

$$\tau_e = \frac{1}{(2\pi f_{max})} \tag{9}$$

where f_{max} and τ_e are the peak frequency in the Bode phase plots and the lifetime of electron, respectively. Consequently, the f_{max} values for Ti/TiO_2 and Ti/TiO_2-$Pb_5S_2I_6$-PDA under visible light irradiation were found to be 5.58 and 1.70 Hz (Fig. 4d), respectively, corresponding to electron lifetimes of 2.85×10^{-2} and 9.30×10^{-2} s, where the longer lifetime corresponds to more efficient charge separation.

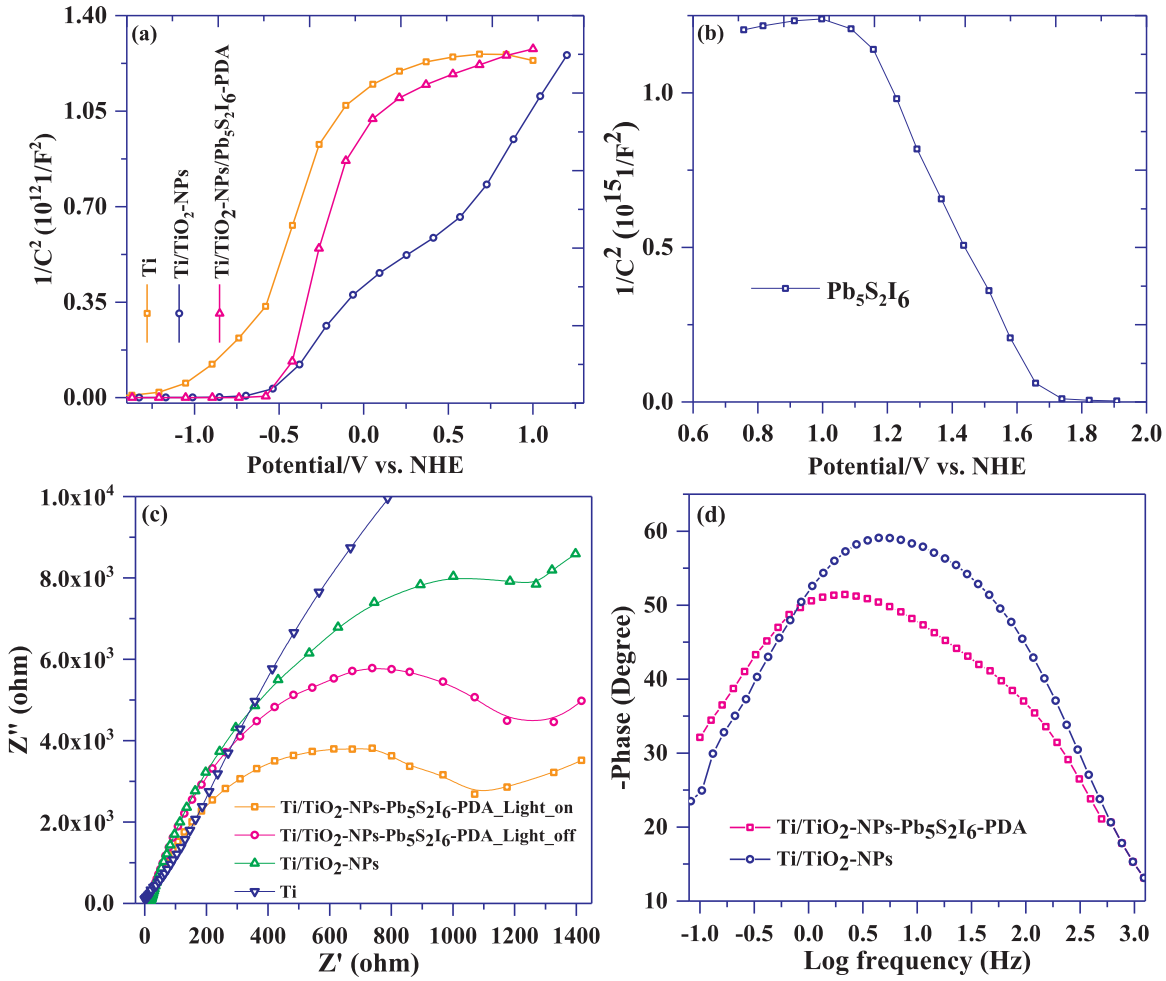

Fig. 4. (a) Mott – Schottky plots collected at 5 kHz for Ti foil, Ti/TiO_2 and Ti/TiO_2-$Pb_5S_2I_6$-PDA and (b) $Pb_5S_2I_6$, (c) EIS Nyquist plots of the Ti foil, Ti/TiO_2 and Ti/TiO_2-$Pb_5S_2I_6$-PDA and Ti/TiO_2-$Pb_5S_2I_6$-PDA under visible light irradiation and (d) Bode phase plots of Ti/TiO_2 and Ti/TiO_2-$Pb_5S_2I_6$-PDA at different frequencies under visible light irradiation.

3.6. The sensing mechanism

The activity of $Pb_5S_2I_6$ as visible-light active agent can be studied using PL, DRS, CV, EIS, amperometric and potentiometric analyses. The heterostructure coated on Ti/TiO_2 support was estimated to be of Type-II. According to the above-mentioned results, the approximate Eg values for Ti/TiO_2, pure $Pb_5S_2I_6$ and Ti/TiO_2-$Pb_5S_2I_6$-PDA were obtained to be 3.36, 1.92 and 2.62 eV, respectively. In addition, $Pb_5S_2I_6$, Ti, Ti/TiO_2 and Ti/TiO_2-$Pb_5S_2I_6$-PDA are p-, n-, n- and n- type semiconductors, respectively (See Fig. 5). Therefore, after making junctions, the electrons in the VB of photoactive $Pb_5S_2I_6$ is excited to the CBs under blue-light irradiation. The E_{CB} and E_{VB} of $Pb_5S_2I_6$ were obtained to be −0.07 and 1.85 eV, respectively. Assuming a type II photocatalytic mechanism for the $Pb_5S_2I_6$ and TiO_2 system, the photogenerated electron would be transferred from the CB of p-type $Pb_5S_2I_6$ to that of n-type TiO_2 by PDA mediator (See Fig. 5). In such charge carrier scheme, the reduction of Cr(VI) to Cr(III) occurring at 1.44 eV vs NHE can easily be conducted at the CB of $Pb_5S_2I_6$. In other words, the potential CB of the $Pb_5S_2I_6$ after the junction is more negative than the potential at which the Cr(VI) reduces to Cr(III). In the meantime, the merged triethanolamine (TEA) anions could efficiently trap the generated holes. In such charge transfer scheme, PDA and $Pb_5S_2I_6$ can effectively absorb the blue light followed by the electron-hole generation because of the dipolar character.

3.7. CCD analysis (Fitting Model and ANOVA)

The "Lack of fit" tests and sequential model sum of squares (Table S2) were considered and the desirable amount of R-values together with the insignificant lack of fit was used to select a quadratic model for further analysis. The investigation on F-values, p-values and model lack of fit obtained by ANOVA was carried out to assess the model significance (Table S3). The P-values less than 0.05 show the significance of corresponding factors or model. The lack-of-fit value higher than 0.05 indicates that the obtained model well describes the experiments and predict the response with no systematic error. Finally, the simplified model was applied in terms of coded factors for predicting the photocurrent of proposed PEC biosensor for the detection of Cr(VI) ions in aqueous media (Eq. (10)):

$$\begin{aligned} R \;=\; & +0.26 - 5.3E - 003X_1 - 2.18E - 003X_2 - 0.043X_3 \\ & + 1.12E003X_1X_2 - 1.24E \\ & -004X_1X_3 + 0.010X_2X_3 - 0.012X_1^2 - 0.029X_2^2 - 0.024X_3^2 \end{aligned} \quad (10)$$

The F-test was used to find the significant effect of individual variables on the photocurrent of proposed PEC biosensor for Cr(VI) ions determination. Well applicability of this model was validated by high F-value (2590.38) obtained. The "Lack of Fit F-value" corresponding to the model applied for the prediction of photocurrent of proposed PEC biosensor for Cr(VI) ions determination was obtained to be 0.085. This value supports the insignificant lack of fit of the model relative to pure

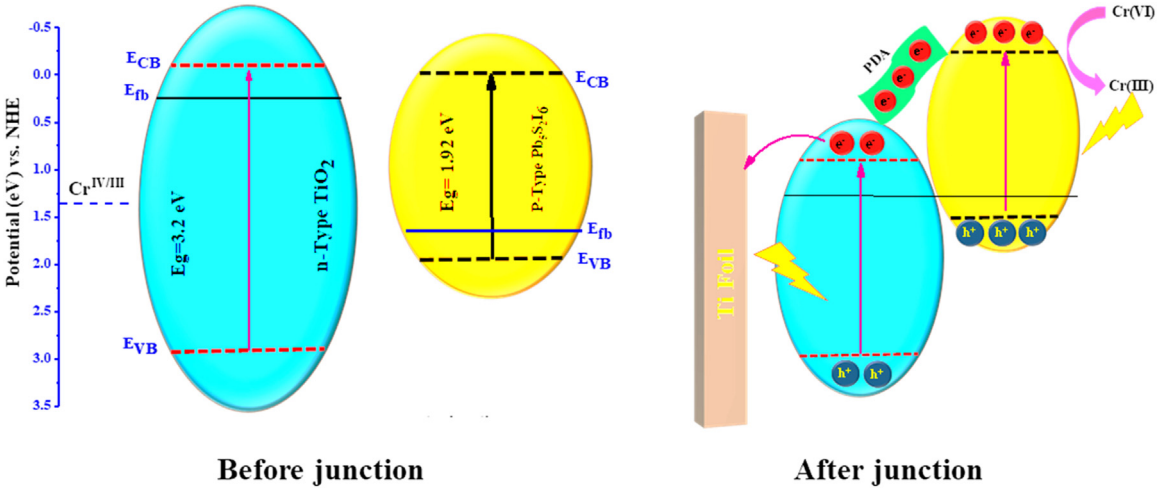

Fig. 5. Band position and proposed PEC mechanism for the detection of Cr(VI).

error. In addition, it approves that the developed model efficiently predict the response. The fact that the values of R^2 (0.9996) and Adj-R^2 (0.9992) are nearly equal to 1.0 indicates well-correlated predicted and observed values (See Table S3). The comparison of predicted photocurrent to that of proposed PEC biosensor experimentally obtained for the determination of Cr(VI) ions (See Fig. S2a) resulted in a good consistency (R^2 = 0.9971). Moreover, adequate precision, mean, standard error, CV% and PRESS confirm the well applicability of developed model for the Cr(VI) ion determination (Table S3). The Leverage (Fig. S2b) is a criterion for assessing the extent to which the fitting quality is affected by each point. Leverage one corresponding to a point indicates its pass through the model. A point of high leverage behave badly because in case of occurring an unexpected error, the model would be strongly influenced by that error. No point was found with leverage value higher than 1.0 (Fig. S2b), which brings us to the conclusion that there exists no outlier or unexpected error in the developed model. The model fit quality was investigated by creating the internally studentized residuals against the predicated photocurrent of proposed PEC biosensor (Fig. S2c), which showed the localization of all data within the limits (with confidence interval of 95%). Moreover, the difference in fits (DFFITS), as a criterion on the level in which each point affects the predicted value, is applied to estimate the model reliability. The values were found to be within the obtained range (Fig. S2d), which can clearly verify the model reliability.

3.8. Optimization condition

The PEC sensing process should be carefully optimized to achieve maximum selectivity and response to Cr(VI) ions. Here, CCD together with desirability function was applied to obtain optimal factors significantly affecting the photocurrent to determine Cr(VI) ions using the designed PEC biosensor. The desirability was set to be 0.0, 0.5 and 1.0 corresponding to its minimum, middle and maximum, respectively. The value obtained nearer to 1.0 corresponds to more optimum condition. Hence, the optimal parameters with desirability of 0.99 were adjusted at 5.0, −0.45 V and 540 nm corresponding to pH, applied potential and radiant light wavelength, respectively (Fig. S3). Moreover, at these conditions, the photocurrent was found to be 0.263 mA.

3.9. 3D plots and effect of variables

The pH of supporting electrolyte importantly played a role in the responses of proposed Ti/TiO_2-$Pb_5S_2I_6$-PDA PEC bioassay. The photocurrent of Ti/TiO_2-$Pb_5S_2I_6$-PDA decreased with increasing pH values over 5.5–8.0 due to the deposition of Cr(III) hydroxide on the photoelectrode surface at pH > 5.5, which makes the catalysts deactivated (Fig. S4a). At lower pHs, the photogenerated electrons of Ti/TiO_2-$Pb_5S_2I_6$-PDA can be easily captured by the protons, which leads to the decrease in the photocurrent. The photocurrent was observed to be maximum at pH 5.0 with high stability while dropping off over higher pHs within the range 5.5–8.0, which is because of more ability of Cr(VI) oxidation in acidic medium as well as the significant photoreduction of Cr(VI) by generated electrons on Ti/TiO_2-$Pb_5S_2I_6$-PDA. Therefore, for being practical in real samples, the pH of detection solution was set at 5.0.

The photocurrent of Ti/TiO_2-$Pb_5S_2I_6$-PDA was studied under different irradiation light sources with dominant wavelengths of 410 nm, 475 nm, 540 nm, 605 nm and 670 nm. As shown in Fig. S4b, Ti/TiO_2-$Pb_5S_2I_6$-PDA irradiated by LED light source with dominant wavelength of 540 nm showed larger photocurrent because of its appropriate band position between blue LED light and Ti/TiO_2-$Pb_5S_2I_6$-PDA. With increase in dominate wavelength of LED light source, the value of photocurrent for Ti/TiO_2-$Pb_5S_2I_6$-PDA showed a decreasing tendency.

3.10. Analytical performance of Ti/TiO_2-$Pb_5S_2I_6$-PDA for Cr(VI) determination

The photocurrent of Ti/TiO_2-$Pb_5S_2I_6$-PDA was measured at various concentrations of Cr(VI) ions in 0.1 M Tris-HCl (pH = 5) buffer solution containing 0.01 M triethanolamine (TEA) at optimal condition (See Fig. 6a). As the concentration of Cr(VI) ions increases, the photogenerated current of Ti/TiO_2-$Pb_5S_2I_6$-PDA increases successively, which effectively permits the photoreduction of Cr(VI) to Cr(III) via photogenerated electrons on Ti/TiO_2-$Pb_5S_2I_6$-PDA because of fitting the band position of Ti/TiO_2-$Pb_5S_2I_6$-PDA with redox potential of Cr(VI)/Cr(III) (1.33 V, NHE). Meanwhile, the merged triethanolamine (TEA) anions efficiently capture the photogenerated holes. A linear proportionality was found between the Cr(VI) ions concentration over 0.01–80.0 μM and the relative photocurrent variation ($\Delta I/I_0$, $\Delta I = I - I_0$, where I and I_0 are the photocurrents after and before adding the Cr(VI) ions, respectively), with R value of 0.999 (See Fig. 6b). The limit of detection (S/N = 3) was determined to be 3.0 nM taken from the response of three times the standard deviation of the response at zero-dose. This value is meaningfully lower than the values obtained using FAAS (~ 0.8 ppb), ICP-MS (~10.0 ppb), WHO (1.9 μM) and electrocatalytic detection (~ 5.2 ppb) as well as higher than that obtained using fluorescence technique. Thus, our method is sensitive enough to screen the amount of Cr (VI) ions in real samples.

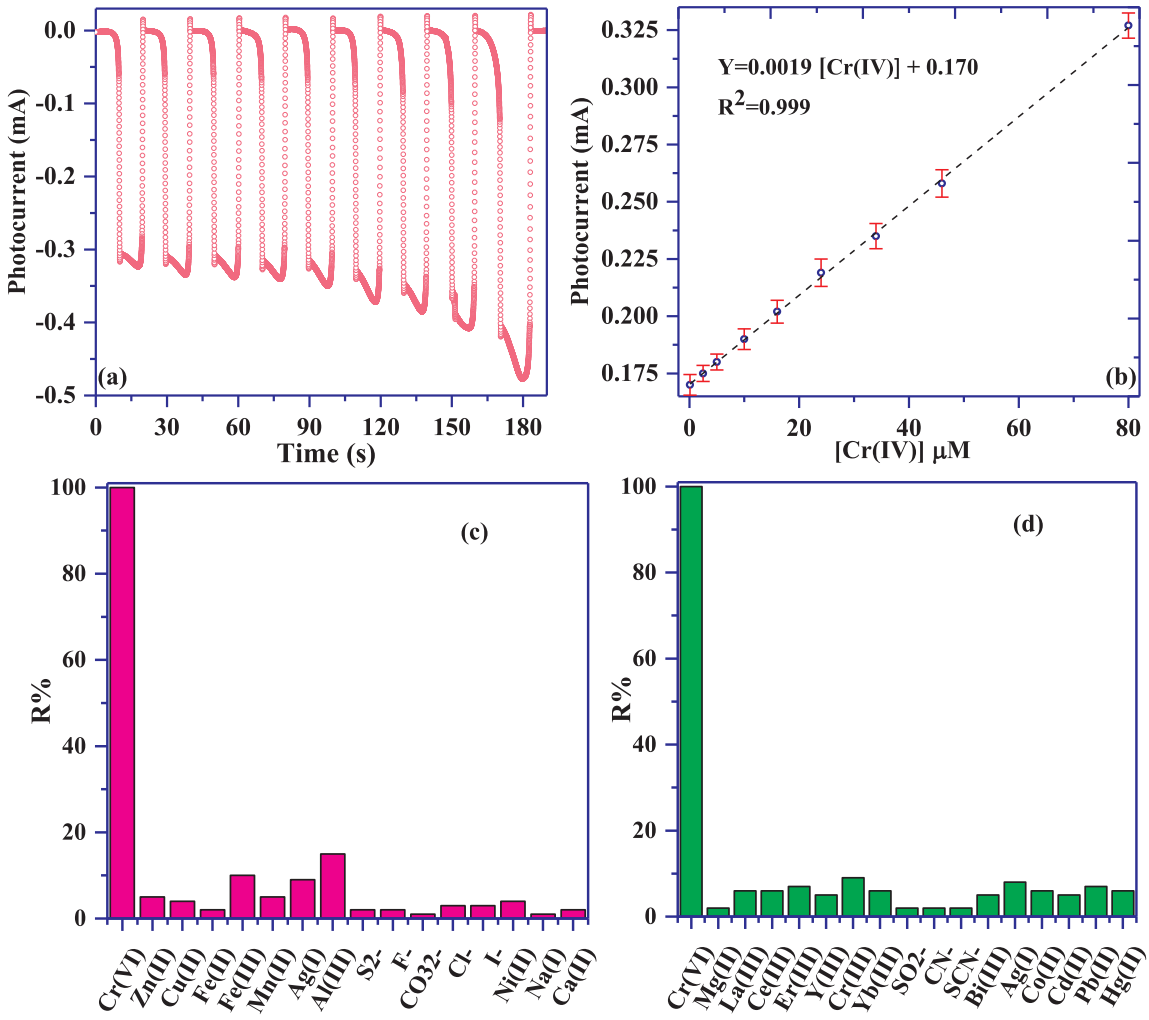

Fig. 6. (a) Photocurrent at Ti/TiO_2-$Pb_5S_2I_6$-PDA in 0.1 M Tris (pH 5) at a bias voltage of −0.45 V after incubation with 0.01–80 μM of Cr(VI) ions, (b) calibration based on PEC response of Ti/TiO_2-$Pb_5S_2I_6$-PDA and Cr(VI) ions concentration from 0.01 to 80 μM and (c) the relative photocurrent density ratio of different interfering solutions on the PEC sensor.

3.11. Selectivity, repeatability and reproducibility of the proposed sensor

To investigate the selectivity of the Ti/TiO_2-$Pb_5S_2I_6$-PDA PEC biosensor, several other ions were selected as interfering agents. The photocurrent density of various interfering agents was measured to study the selectivity of our sensor. The value of R (%)was calculated as follows (Chen et al., 2018):

$$R(\%) = \frac{I_c - I_0}{I_{Cr(VI)} - I_0} \quad (11)$$

where I_0 was the photocurrent density in 10 mM Tris solution, $I_{Cr(VI)}$ and I_c were the photocurrent densities in 30 μM Cr(VI) and 100 μM interfering solution, respectively. The R (%) value for 30 μM Cr(VI) was found to be 100%, and the values corresponding to other interfering agents were obtained by Eq. (11). Consequently, all R (%) values were found to be not higher than 15% in 100 μM interfering solutions (Fig. 6c and d), which is due to the specificity of band position of selected materials.

The repeatability of the Ti/TiO_2-$Pb_5S_2I_6$-PDA photoelectrode during a day and over days was examined by illuminating the same electrode for five repetitive chronoamperometric experiments at potential of −0.45 V versus Ag/AgCl for the detection of 30 μM Cr(VI). Relative standard deviation (RSD) values of 1.7% and 1.9% were observed corresponding to inter- and intra-day analyses, respectively, reflecting good repeatability of the sensor.

The reproducibility of proposed PEC sensing method inter- and intra-day was tested by preparing five Ti/TiO_2-$Pb_5S_2I_6$-PDA electrodes and performing the chronoamperometric experiment for the detection of 30 μM Cr(VI) at potential of −0.45 V versus Ag/AgCl where irradiated by blue light. For the designed five electrodes, the RSD values of 2.2% and 2.5% were found during a day and over days, respectively, which their photocurrent responses demonstrate their reproducibility.

3.12. Real sample analysis

To investigate the practical feasibility of the Ti/TiO_2-$Pb_5S_2I_6$-PDA biosensor, three real samples including wastewater, hair color and tomato juice were collected to determine Cr(VI) using standard addition way (See Table S4 for the various contents of Cr(VI)) in the real samples (n = 3.0). The recoveries were obtained to be in the range of 97.15–103.25%. In the meantime, the values of RSD (from 0.8% to 3.8%) were calculated to test the accuracy of measurements. The results suggested that the Ti/TiO_2-$Pb_5S_2I_6$-PDA biosensor is excellently accurate and precise, and promisingly applicable to quantify the Cr(VI) ions concentration in these real samples.

4. Conclusion

We successfully designed a $Pb_5S_2I_6$-containing PDA-coated nanoporous TiO_2 to fabricate an efficient visible-light-driven PEC sensor for

Cr(VI) ions detection. The structural, optical and PEC properties of the sensor were studied in addition to the determination of its specific energy levels ($V_{VB}/V_{CB}/V_{fb}$). It was found that the Ti/TiO_2 electrode ideally couples with $Pb_5S_2I_6$ as an ideal photoactive material, achieving good PEC properties. In contrast to enzyme-based PEC biosensors, our method is suitable and easy to apply with no need to elaborate pre-treatment. The photo-absorption of $Pb_5S_2I_6$ and PDA over wide wavelength range of visible-light was enhanced with efficient incorporation of TiO_2 to overall achieve a high visible-light-driven response. The fabricated sensor could be satisfactorily applied to determination of Cr (VI) ions in real samples. This strategy showed high sensitivity, good selectivity, acceptable repeatability and reproducibility and stability, and we believe that this work will provide a prosperous future road map for various PEC bioassays, which will extend the viewpoint in the design and construction of ultrasensitive PEC bioanalytical protocols. In addition, the developed PEC sensor is advantageous because it has no common drawback reported in previous works and it is easy to amplify the signal for the sensitive bioassay of Cr(VI) in real sample due to the effective regeneration of signaling species in a separated environment.

Acknowledgments

Yasouj University, Iran, is acknowledged for supporting this work.

Novelty statement

This article reports the design of a novel PEC sensor based on ideal photoactive chalco-halide $Pb_5S_2I_6$ p-type heterostructure. $Pb_5S_2I_6$ was synthesized by a rapid hydrothermal method at low temperature (160 °C) in hydrochloride acid media followed by its incorporation into polydopamine (PDA) as reactive biointerface, through a facile in situ electropolymerization method, coated on nonporous TiO_2 grown on Ti foil. This unique $Pb_5S_2I_6$ catalyst-based PEC bioassay was constructed for the detection of low-abundant Cr(VI) ion in real samples.

Appendix A. Supplementary material

Supplementary data associated with this article can be found in the online version at doi:10.1016/j.bios.2019.02.042.

References

Arvand, M., Ghodsi, N., Zanjanchi, M.A., 2016. Biosens. Bioelectron. 77, 837–844.
Asfaram, A., Ghaedi, M., Hajati, S., Goudarzi, A., Bazrafshan, A.A., 2015. Spectrochim. Acta Part A: Mol. Biomol. Spectrosc. 145, 203–212.
Azad, F.N., Ghaedi, M., Dashtian, K., Hajati, S., Pezeshkpour, V., 2016. Ultrason. Sonochem. 31, 383–393.
Biyareh, M.N., Rezvani, A.R., Dashtian, K., Montazerozohori, M., Ghaedi, M., Asl, A.M., White, J., 2018. IEEE Sens. J.
Challagulla, S., Nagarjuna, R., Ganesan, R., Roy, S., 2016. ACS Sustain. Chem. Eng. 4 (3), 974–982.
Chen, J., Gao, P., Wang, H., Han, L., Zhang, Y., Wang, P., Jia, N., 2018. J. Mater. Chem. C 6 (15), 3937–3944.
Dashtian, K., Ghaedi, M., Shirinzadeh, H., Hajati, S., Shahbazi, S., 2018a. Chem. Eng. J. 339, 189–203.
Dashtian, K., Mosleh, S., Ghaedi, M., Jannesar, R., 2018b. New J. Chem.
Fang, T., Yang, X., Zhang, L., Gong, J., 2016. J. Hazard. Mater. 312, 106–113.
Feng, J., Huang, H., Yu, S., Dong, F., Zhang, Y., 2016. Phys. Chem. Chem. Phys. 18 (11), 7851–7859.
Habibi-Yangjeh, A., Shekofteh-Gohari, M., 2017. Sep. Purif. Technol.
Iyengar, A., 2017. ACS Appl. Mater. Interfaces.
Jang, J.S., Ahn, C.W., Won, S.S., Kim, J.H., Choi, W., Lee, B.-S., Yoon, J.-H., Kim, H.G., Lee, J.S., 2017. J. Phys. Chem. C 121 (28), 15063–15070.
Jiang, Z., Sun, H., Wang, T., Wang, B., Wei, W., Li, H., Yuan, S., An, T., Zhao, H., Yu, J., 2018. Energy Environ. Sci. 11 (9), 2382–2389.
Khare, P., Bhati, A., Anand, S.R., Gunture, Sonkar, S.K., 2018. ACS Omega 3 (5), 5187–5194.
Kheirandish, S., Ghaedi, M., Dashtian, K., Heidari, F., Pourebrahim, F., Wang, S., 2017a. Int. J. Biol. Macromol. 102, 181–191.
Kheirandish, S., Ghaedi, M., Dashtian, K., Jannesar, R., Montazerozohori, M., Pourebrahim, F., Zare, M.A., 2017b. J. Colloid Interface Sci.
Kheirandish, S., Ghaedi, M., Dashtian, K., Pourebrahim, F., 2017c. Ultrason. Sonochem.
Li, J., Li, X., Zhao, Q., Jiang, Z., Tadé, M., Wang, S., Liu, S., 2018. Polydopamine-assisted decoration of TiO2 nanotube arrays with enzyme to construct a novel photoelectrochemical sensing platform. Sens. Actuators B: Chem. 255, 133–139.
Li, X., Zhu, L., Zhou, Y., Yin, H., Ai, S., 2017. Anal. Chem. 89 (4), 2369–2376.
Lin, Z., Li, M., Lv, S., Zhang, K., Lu, M., Tang, D., 2017. J. Mater. Chem. B 5 (43), 8506–8513.
Liu, X., Liu, P., Tang, Y., Yang, L., Li, L., Qi, Z., Li, D., Wong, D.K., 2018. Biosens. Bioelectron. 112, 193–201.
Liu, Y., Ma, H., Zhang, Y., Pang, X., Fan, D., Wu, D., Wei, Q., 2016. Biosens. Bioelectron. 86, 439–445.
Ma, Z.-Y., Xu, F., Qin, Y., Zhao, W.-W., Xu, J.-J., Chen, H.-Y., 2016. Anal. Chem. 88 (8), 4183–4187.
Moakhar, R.S., Goh, G.K.L., Dolati, A., Ghorbani, M., 2017. Appl. Catal. B: Environ. 201, 411–418.
Mosleh, S., Rahimi, M., Ghaedi, M., Dashtian, K., 2016a. Ultrason. Sonochem. 32, 387–397.
Mosleh, S., Rahimi, M., Ghaedi, M., Dashtian, K., Hajati, S., 2016b. RSC Adv. 6 (21), 17204–17214.
Mosleh, S., Rahimi, M.R., Ghaedi, M., Dashtian, K., Hajati, S., 2016c. RSC Adv. 6 (68), 63667–63680.
Mousavinia, S.E., Hajati, S., Ghaedi, M., Dashtian, K., 2016. Phys. Chem. Chem. Phys. 18 (16), 11278–11287.
Padhi, D.K., Baral, A., Parida, K., Singh, S.K., Ghosh, M.K., 2017. J. Phys. Chem. C 121 (11), 6039–6049.
Padhi, D.K., Parida, K., 2014. J. Mater. Chem. A 2 (26), 10300–10312.
Pathak, P., Podzorski, M., Bahnemann, D., Subramanian, V.R., 2018. J. Phys. Chem. C.
Pirhashemi, M., Habibi-Yangjeh, A., 2015. Ceram. Int. 41 (10), 14383–14393.
Ren, R., Cai, G., Yu, Z., Zeng, Y., Tang, D., 2018. Anal. Chem. 90 (18), 11099–11105.
Rezaei, B., Khosropour, H., Ensafi, A.A., Dinari, M., Nabiyan, A., 2015. RSC Adv. 5 (92), 75756–75765.
Ruan, Y.-F., Zhang, N., Zhu, Y.-C., Zhao, W.-W., Xu, J.-J., Chen, H.-Y., 2017. Anal. Chem. 89 (15), 7869–7875.
Shu, J., Qiu, Z., Lv, S., Zhang, K., Tang, D., 2018. Anal. Chem. 90 (4), 2425–2429.
Shu, J., Qiu, Z., Zhou, Q., Lin, Y., Lu, M., Tang, D., 2016. Anal. Chem. 88 (5), 2958–2966.
Shu, J., Tang, D., 2017. Chemistry Asian J. 12 (21), 2780–2789.
Sui, C., Wang, T., Zhou, Y., Yin, H., Meng, X., Zhang, S., Waterhouse, G.I., Xu, Q., Zhuge, Y., Ai, S., 2019. Biosens. Bioelectron. 127, 38–44.
Tabatabaei, N., Dashtian, K., Ghaedi, M., Sabzehmeidani, M.M., Ameri, E., 2018. New J. Chem. 42 (12), 9720–9734.
Thulasi-Varma, C.V., Rao, S.S., Ikkurthi, K.D., Kim, S.-K., Kang, T.-S., Kim, H.-J., 2015. J. Mater. Chem. C 3 (39), 10195–10206.
Wang, G.-L., Shu, J.-X., Dong, Y.-M., Wu, X.-M., Zhao, W.-W., Xu, J.-J., Chen, H.-Y., 2015. Anal. Chem. 87 (5), 2892–2900.
Wang, H., Zhang, B., Zhao, F., Zeng, B., 2018. ACS Appl. Mater. Interfaces 10 (41), 35281–35288.
Wang, K., Zhang, R., Sun, N., Li, X., Wang, J., Cao, Y., Pei, R., 2016. ACS Appl. Mater. Interfaces 8 (39), 25834–25839.
Xie, X., Mao, C., Liu, X., Tan, L., Cui, Z., Yang, X., Zhu, S., Li, Z., Yuan, X., Zheng, Y., 2018. ACS Cent. Sci.
Xue, J., Gao, C., Zhang, L., Cui, K., He, W., Yu, J., 2018. J. Mater. Chem. B.
Yu, Z., Tang, Y., Cai, G., Ren, R., Tang, D., 2018. Anal. Chem. 91 (2), 1222–1226.
Zhang, D., Wang, F., Cao, S., Duan, X., 2018. RSC Adv. 8 (11), 5967–5975.
Zhang, X., Li, H., Wang, S., Fan, F.-R.F., Bard, A.J., 2014. J. Phys. Chem. C 118 (30), 16842–16850.
Zhu, Y.-C., Zhang, N., Ruan, Y.-F., Zhao, W.-W., Xu, J.-J., Chen, H.-Y., 2016. Anal. Chem. 88 (11), 5626–5630.